A Generic Hybrid Model for the Simulation of Three-dimensional Bulk Elastodynamics for Use in Non-Destructive Evaluation

W. Choi, E. A. Skelton, J. Pettit, M. J. S. Lowe and R. V. Craster

***Abstract*—A three-dimensional generic hybrid model is developed for the simulation of elastic waves in applications in Non-Destructive Evaluation that efficiently links different solution strategies but, crucially, is independent of the particular schemes employed. This is an important step forward in facilitating rapid and accurate large-scale simulations and this advances the two-dimensional generic hybrid methodology recently developed by the authors. The hybrid model provides an efficient and effective tool for creating highly accurate simulations that model the wave propagation and scattering, enabling the interpretation of inspection data; the new methodology is verified against other numerical simulations. Furthermore, its deployment to simulate wave reflection from side-drilled holes, comparing the results with experimental measurements, provides a realistic demonstration as well as further validation.**

***Index Terms*—Nondestructive evaluation, Simulation, Hybrid model, Elastic wave**

I. Introduction

Ultrasonic inspection is economic, versatile and safe, and is widely used across a broad range of industries. Its usage is expanding as new inspection capabilities are emerging together with advancing requirements for the inspection of safety-critical components. As this demand increases and applications broaden, there is a consequent increase in complexity for inspection procedures. Accurately, and rapidly, simulating such inspection procedures is of considerable benefit to estimate or confirm inspection results, to validate proposed inspections, and, as a result, to increase confidence in ultrasonic Non-Destructive Evaluation (NDE).

In ultrasonic NDE the measurement and modelling of wave scattering from discontinuities is essential when trying to detect or size cracks in engineering structures. While the problem is fundamentally an inverse one, to identify and interpret defects from measured signals, the practical deployment of NDE uses forward calculations and simulations as the basis to make the interpretations. There are numerous existing techniques to model this scattering, each with some relative advantage or disadvantage, and the current state-of-the-art is reviewed and then how the hybrid methodology is positioned within this existing landscape is illustrated.

Modelling wave scattering phenomena using analytical techniques yields physical interpretation and meaningful representations; these techniques deliver results reliably, although such models are typically limited to cracks with well-defined planar or regular geometries. Semi-analytic techniques based upon limitations in frequency such as the Kirchhoff approximation [1], the Geometric Theory of Diffraction (GTD) [2], and Physical Theory of Diffraction (PTD) [3] are also popular and widely used in NDE [4], [5]: These have the advantage that irregular geometries can then be considered. However, there are difficulties dealing with wave behaviour with respect to defects described by rough or complex geometries.

Numerical modelling tools such as the Finite Element (FE) method are naturally appealing in this context and have also been developed for simulating ultrasonic waves in NDE, for example [6]–[9]. In contrast to analytic methods, numerical tools are particularly good at modelling irregular geometries and thus widely used in practical applications to deal with ultrasonic waves in real complex structures. However the FE modelling of such geometries requires highly resolved meshes that increase the relative number of elements and consequently the computational burden increases dramatically. In addition, if the ultrasonic wave travels a long distance, it often requires very large domains to be treated, and further worsen this issue by increasing the number of nodes. Unfortunately, simulating an infinite domain by truncation to a finite computational domain introduces further complications by requiring a boundary condition, or absorbing region, to avoid unwanted reflection from the artificially introduced boundaries, and typically this is modelled by a wave-absorbing layer [10]. To simulate an infinite medium, the truncated finite region is surrounded by an absorbing layer and, annoyingly often, the size of this absorbing region is larger than the main domain. The efficiency of these absorbing layer methods has been investigated and improved by many researchers [11]–[15], but FE methods still experience computational difficulties due to sheer model size, particularly in three dimensions.

Each of these techniques has some advantage or disadvantage, so it is attractive to try to maximise efficiency by developing hybrid methods that combine the best aspects of these different modelling techniques. FE and analytic methods, for example, have different merits and so researchers have combined them to generate more efficient tools for estimating wave

Manuscript received March 11, 2016

This work was supported in part by Rolls-Royce Plc, Derby, U.K. and in part SIMPOSIUM project: the European Community's Seventh Framework Program (FP7/2007-2013) under Grant 285549

W. Choi and M. J. S. Lowe are with the Department of Mechanical Engineering, Imperial College London, SW7 2AZ, U.K.

W. Choi is currently with Center for Safety Measurement, KRISS, Daejeon, 34113, Rep. of Korea. (e-mail: w.choi@kriss.re.kr)

J. Pettit is with Rolls-Royce Nuclear, Derby, DE21 7XX, U.K.

E. A. Skelton and R. V. Craster are with the Department of Mathematics, Imperial College London, SW7 2AZ, U.K.

propagation and scattering. Many hybrid methods have been successfully developed [8], [16]–[18], but they are primarily for particular techniques or processes. Thus the methods need to be modified in order to have the flexibility to be rapidly and easily applied to different techniques and problems. To overcome this, and to generate a flexible methodology, a generic hybrid method (in two-dimensions) has been developed by the authors' research team at Imperial College [19], that allows one to connect two different techniques using a hybrid interface that is independent of the techniques to be linked. The flexibility is important when using commerical FE codes, that are certified for particular industrial uses, as there is no access to the source code: all numerical examples presented here are generated with ABAQUS [20] as an example FE code.

The advantages of the hybrid approach come to the fore in three-dimensional (3D) problems, but it is not straightforward to extend the 2D generic hybrid model to 3D. Technical challenges arise that must be overcome and they are considered within this article. Verification of the model is also presented by detailed comparison of simulations with alternative numerical results, and a realistic demonstration with further validation by comparison with experimental measurements on a realistic industrial example.

In this paper, firstly the basic background of the 3D hybrid method is introduced, and methodologies of the hybrid interface and its application to numerical FE model are described in Section III. Comprehensive numerical verification and experimental validation then follows in sections IV and V. Then some concluding remarks are drawn together in section VI.

II. Background

Recently, a generic hybrid method has been developed for ultrasonic NDE problems [19] that allows separately modelled regions to be linked, independent of the modelling procedures used in either domain. The concept will be briefly introduced here, but for full details see [19].

A pulse-echo NDE setup as, for example, shown in Fig. 1(a) is modelled with the source and defect located within two separate small domains as shown in Fig. 1(b). For the displacement potential of a compressional wave, ϕ, travelling from the Source domain (Region 1) to the Defect domain (Region 2), the two regions are linked via an integral formula in the frequency domain,

$$\phi(\mathbf{r}_2) = \int_{S_1} [\phi(\mathbf{r}_1)\nabla G_\phi(\mathbf{r}_2|\mathbf{r}_1) - G_\phi(\mathbf{r}_2|\mathbf{r}_1)\nabla\phi(\mathbf{r}_1)] \cdot \mathbf{n}\mathrm{d}S_1 \tag{1}$$

where $G_\phi(\mathbf{r}_2|\mathbf{r}_1)$ is the Green's function as in Eq. (5), $\mathbf{r}_1$ and $\mathbf{r}_2$ are position vectors of points on the boundary of the Source domain (Region 1), S_1, and points in the Defect domain (Region 2), respectively, and $\mathbf{n}$ is the normal to the Source domain boundary. The physical quantities in Region 2 such as displacement and stress are readily calculated from the potential, which will be explained in the next section. An alternative approach to link the two regions via an integral formula could be to use tensor Green's functions, as in say Eq. (4.77) of [21] in which the displacement at Region 2 could also be computed directly from displacement and stress at Region 1; both approaches should produce identical results. In this work we consider isotropic elastic media, which enables the necessary domain-linking to be based on appropriate Greens functions written in terms of displacement potentials, and we have chosen this option. For the general case of anisotropic elastic media, the problem could be formulated instead in terms of tensor Greens functions that directly link stresses and displacements, and we would expect this to require similar computational resource. For time domain prediction, the Fast Fourier Transform (FFT) and inverse FFT (IFFT) techniques are used within the hybrid interface. Wave reflection from the defect travelling back to the source domain (or elsewhere) is determined using the identical process but from the Defect to the Source domain.

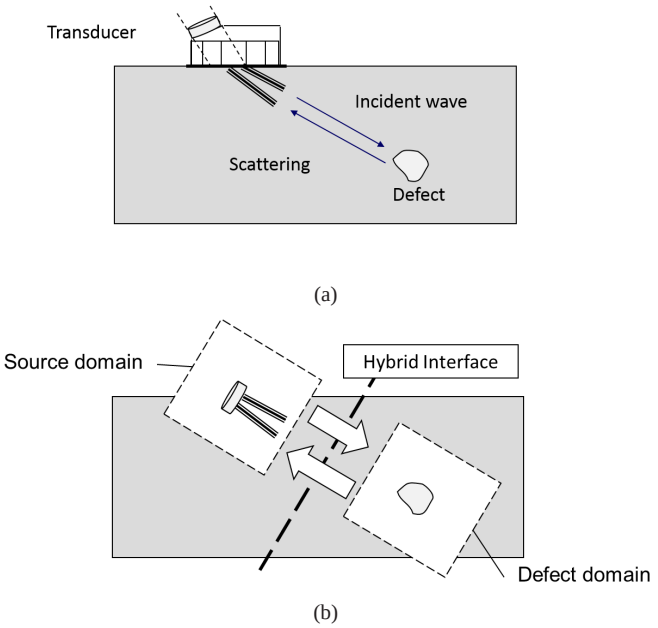

Fig. 1: Generic hybrid concept for the simulation of ultrasonic pulse-echo NDE; (a) illustration of the NDE setup, (b) Hybrid model using a Source domain and a Defect domain to account for the complexity of the transduction and scattering respectively, while the propagation of the waves between these domains is handled by the equations of the analytic model

The implementation of the hybrid interface depends solely on the linking of field quantities at the exterior boundaries of any chosen local domains. This can be the Source and Defect domains, as in the example in Fig. 1(b), or could include others: for example it is straightforward to model the detection of scattered waves at a receiver location that is separated from the transmitter, such as in a pitch-catch NDE setup. Within each of these domains there is no restriction of the choice of modelling technique, provided it can deliver and receive the field quantities at the exterior of the domain. Here we use the FE technique within the domains, to take advantage of its superior capability to model the complexity of the behaviour at the transducer and at the defect, but in principle any other technique that is appropriate for the local behaviour could be used. We also choose to use a commercially available FE code for these domains, which provides the advantage that the

hybrid model can be accessible immediately to NDE modellers who may be restricted in their choice of modelling tools. This is frequently the case in industry where decisions concerning licensing or qualification approval can be very limiting. The possibility to use any appropriate local model also allows such users to take advantage of their familiarity and developed skills for their specific codes.

An important characteristic of the local domain is that the exterior boundary itself must not affect the calculations. When using FE modelling, this means that it is necessary to allow waves to radiate from the domain without interacting with the boundary. As discussed earlier, there are well-developed techniques to deal with unwanted reflections from artificially introduced boundaries. Here, in keeping with our motivation to open the methodology to a wide range of both academic and industrial modellers, we use an absorbing region that is easily implemented using the standard features of commercial FE codes [14].

III. A GENERIC WAVE PROPAGATOR IN THREE DIMENSIONS

A. *Linking scheme*

For the hybrid interface described here, displacement potentials and their derivatives are assumed to be known on the boundary of Region 1 and we work with those potentials rather than directly with the stresses and displacements. For a 3D wave field, the longitudinal potential ϕ is a scalar function whilst the shear potential, in contrast to a 2D problem, is a vector quantity $\boldsymbol{\psi} = (\psi, \chi, \eta)$, with its three components representing shear polarization in three orthogonal directions. In general this results in 4 potentials to represent the 3 components of the displacement; this is over-determined and to remove any ambiguity a gauge condition, $\nabla \cdot \boldsymbol{\psi} = 0$, is required [22]. For notational convenience dimensionless variables are used in the following analysis. Thus lengths are scaled with some length h appropriate to the geometry, times are scaled with h/C_T, frequencies are scaled with C_T/h and stresses with the Lamé coefficient $\mu = \rho C_T^2$. The dimensionless displacements follow from the potentials using

$$\mathbf{u} = \nabla\phi + \nabla \times \boldsymbol{\psi}, \tag{2}$$

and the potentials satisfy the homogeneous Helmholz equations,

$$\nabla^2\phi + \omega^2\gamma^2\phi = 0, \tag{3}$$

$$\nabla^2\psi + \omega^2\psi = 0,\ \nabla^2\chi + \omega^2\chi = 0, \text{ and } \nabla^2\eta + \omega^2\eta = 0, \tag{4}$$

where $\gamma = C_T/C_L$, the ratio of the shear and compressional wavespeeds.

Given the potentials and their derivatives on the boundary of Region 1 (the Source domain in Fig. 1(b)), the potential of the incident P-wave field ϕ, for example, is determined on the boundary of Region 2 (the Defect domain in Fig. 1(b)), as in Eq. (1), in which the Green's function for the compressional potential in 3D is

$$G_\phi(\mathbf{r}_2|\mathbf{r}_1) = \frac{1}{4\pi}\frac{e^{-i(\omega\gamma|\mathbf{r}_2-\mathbf{r}_1|)}}{|\mathbf{r}_2-\mathbf{r}_1|}. \tag{5}$$

The other components of the potentials are similarly calculated, all using the same single Green's function based on the shear wave speed. Hence

$$G_\psi(\mathbf{r}_2|\mathbf{r}_1) = G_\chi(\mathbf{r}_2|\mathbf{r}_1) = G_\eta(\mathbf{r}_2|\mathbf{r}_1) = \frac{1}{4\pi}\frac{e^{-i(\omega|\mathbf{r}_2-\mathbf{r}_1|)}}{|\mathbf{r}_2-\mathbf{r}_1|}. \tag{6}$$

Thus computationally only two separate Green's functions are required to be evaluated and stored. Regions 1 and 2 can in general be any shape but here, for simplicity of exposition, it is assumed that they are both cuboids whose edges are parallel to the x, y or z axes. Determining the potentials, and their gradients, on the boundary is straightforward as they are found using the potential-displacement relations and the stress-strain constitutive relations of an elastic material.

B. *Cases defined by displacements and stresses*

The input to, and output from, the hybrid interface can be either displacements or stresses or both, these being the typical outputs of many commercial numerical simulation tools. In this paper it is assumed that both displacements and stresses are available to be input to the hybrid interface and that both are required to be calculated on the Region 2 boundary as the output, but the output could be in any other format obtained from the potentials there. With displacement and/or stress input and/or output the hybrid process consists of three steps: firstly, to obtain the potentials and their normal derivatives from the available data on the Region 1 boundary, secondly to implement the integral equation to calculate potentials on the Region 2 boundary, as described above, and thirdly to calculate the output displacements and/or stresses on the Region 2 boundary from the available values of potentials there. For reference, the equations of motion are listed in dimensionless form in Appendix A. Making use of these dimensionless variables the additional first and third steps are described below:

1) Potentials and their normal derivatives on the Region 1 boundary: The P-wave potential ϕ is obtained by taking the divergence of Eq. (2), using the Helmholtz Eq (3) to replace $\nabla^2\phi$, and Eqs. (23) – (25) to rewrite the $\nabla \cdot \boldsymbol{u}$ term in terms of the dimensionless stresses τ (see Appendix A for details):

$$\phi = \frac{\tau_{xx} + \tau_{yy} + \tau_{zz}}{\omega^2(4\gamma^2 - 3)}. \tag{7}$$

Similarly, expressions for the shear potentials are obtained by taking the curl of Eq. (2) and using the Helmholtz Eqs. (4):

$$\psi = \frac{1}{\omega^2}\left(\frac{\partial u_z}{\partial y} - \frac{\partial u_y}{\partial z}\right), \quad \chi = \frac{1}{\omega^2}\left(\frac{\partial u_x}{\partial z} - \frac{\partial u_z}{\partial x}\right), \quad \text{and} \quad \eta = \frac{1}{\omega^2}\left(\frac{\partial u_y}{\partial x} - \frac{\partial u_x}{\partial y}\right). \tag{8}$$

However, in order to make use only of values on the boundary any normal derivatives are eliminated using the shear stress definitions (26) – (28). For example, on the constant x plane surfaces of the cuboid, for which derivatives with respect to y

and z are available:

$$\psi = \frac{1}{\omega^2}\left(\frac{\partial u_z}{\partial y} - \frac{\partial u_y}{\partial z}\right), \quad \chi = \frac{1}{\omega^2}\left(2\frac{\partial u_x}{\partial z} - \tau_{xz}\right), \quad \text{and} \quad \eta = \frac{1}{\omega^2}\left(\tau_{xy} - 2\frac{\partial u_x}{\partial y}\right). \tag{9}$$

The shear potentials on the other surfaces of the cuboid are derived in a similar manner and, for reference, are listed as Eq. (29) and (30) in Appendix. B.

Normal derivatives of the potentials are also required. For the P-wave potential ϕ, Eq. (7) is formally differentiated and Eqs. (20) – (28) are used to eliminate the normal derivatives in favour of appropriate tangential derivatives. For example, on the constant x surfaces of the cuboid the normal derivative is $\partial\phi/\partial x$ which is evaluated from the values on the surface as

$$\frac{\partial \phi}{\partial x} = \frac{-1}{\omega^2}\left(\frac{\partial \tau_{xy}}{\partial y} + \frac{\partial \tau_{xz}}{\partial z} - 2\left(\frac{\partial^2 u_x}{\partial y^2} + \frac{\partial^2 u_x}{\partial z^2}\right) - \omega^2 u_x\right). \tag{10}$$

Similarly, the normal derivatives of the shear potentials are obtained on the constant x surface as

$$\frac{\partial \psi}{\partial x} = \frac{1}{\omega^2}\left(\frac{\partial \tau_{xz}}{\partial y} - \frac{\partial \tau_{xy}}{\partial z}\right), \tag{11}$$

$$\frac{\partial \chi}{\partial x} = \frac{1}{\omega^2}\left(\omega^2 u_z + \frac{\partial \tau_{yz}}{\partial y} + \frac{\partial \tau_{xx}}{\partial z} + 2\frac{\partial^2 u_z}{\partial z^2}\right), \tag{12}$$

$$\frac{\partial \eta}{\partial x} = \frac{-1}{\omega^2}\left(\omega^2 u_y + \frac{\partial \tau_{yz}}{\partial z} + \frac{\partial \tau_{xx}}{\partial y} + 2\frac{\partial^2 u_y}{\partial y^2}\right). \tag{13}$$

Normal derivatives of potentials on surfaces of constant y and z can also be obtained in the same manner, and expressions for them are presented as Eqs. (31) – (38) in Appendix B.

2) Displacements and stresses on the Region 2 boundary: The integral equations (such as Eq. (1)) can, in theory, estimate the potentials anywhere outside Region 1, and thus displacements and stresses on the boundary of Region 2 are calculated from the potentials and their derivatives. In case that only displacement input is required for the numerical simulation on Region 2, the displacement can be obtained from the values of the potentials on, and near, Region 2 by numerical approximation of the first derivatives in Eq. (2). However, it may be preferred to use force as excitation to the simulation, as in Section V.C, and, in this case, stresses on the region boundary can be used as the excitation, which are defined in terms of first derivatives of displacements or, as in the present method, in terms of the second derivatives of potentials. On the planar surfaces of the Region 2 boundary, the in-plane derivatives are approximated numerically to high order by using more points. For the derivatives in the normal direction, only points on one parallel plane inside the boundary and one parallel plane outside the boundary are evaluated, in order to keep the problem to a manageable size. However, more than three points would be required for higher order approximations. Thus, it is convenient to replace normal derivatives by appropriate tangential derivatives wherever possible, as described in the next paragraph. The spacing between the parallel planes can however be made small to ensure the accuracy of the approximation for any remaining normal derivatives.

Stresses are calculated at points on the surface of a cuboid as follows: for constant x surfaces, the three stresses τ_{xx}, τ_{yy} and τ_{zz} in Eqs. (23) – (25) are rewritten in terms of $\nabla \cdot \boldsymbol{u}$ to formally remove $\partial u_x/\partial x$ terms and then, after making use of Eq. (3), they are expressed using only tangential derivatives as,

$$\tau_{xx} = -\omega^2\phi - 2\left(\frac{\partial u_y}{\partial y} + \frac{\partial u_z}{\partial z}\right), \tag{14}$$

$$\tau_{yy} = -\omega^2\gamma^2(\gamma^{-2} - 2)\phi + 2\frac{\partial u_y}{\partial y}, \tag{15}$$

$$\tau_{zz} = -\omega^2\gamma^2(\gamma^{-2} - 2)\phi + 2\frac{\partial u_z}{\partial z}, \tag{16}$$

where the displacement derivatives are calculated by differentiating Eq. (2). The shear stress component τ_{xy} is obtained by substituting Eq. (2) into Eqs. (26) – (28) and eliminating the second derivatives with respect to x of χ and η using Helmholtz equation (4),

$$\tau_{xy} = 2\frac{\partial^2\phi}{\partial x \partial y} + \left(2\frac{\partial^2}{\partial y^2} + \frac{\partial^2}{\partial z^2} + \omega^2\right)\eta + \frac{\partial^2\psi}{\partial x \partial z} - \frac{\partial^2\chi}{\partial y \partial z}. \tag{17}$$

The remaining first order derivatives with respect to x are evaluated numerically. The other stresses are obtained in the similar manner:

$$\tau_{xz} = 2\frac{\partial^2\phi}{\partial x \partial z} + \frac{\partial^2\eta}{\partial y \partial z} - \left(\frac{\partial^2}{\partial y^2} + 2\frac{\partial^2}{\partial z^2} + \omega^2\right)\chi - \frac{\partial^2\psi}{\partial x \partial y}, \tag{18}$$

$$\tau_{yz} = 2\frac{\partial^2\phi}{\partial y \partial z} - \frac{\partial^2\eta}{\partial x \partial z} + \left(\frac{\partial^2}{\partial z^2} - \frac{\partial^2}{\partial y^2}\right)\psi + \frac{\partial^2\chi}{\partial x \partial y}. \tag{19}$$

Displacements and stresses on the surfaces with constant y and z can be obtained in a similar manner, and expressions for them are given as Eqs. (39) – (51) in Appendix C.

IV. Numerical verification

In this section we report a numerical verification of the 3D hybrid method using FE models in two local domains, although noting, as discussed earlier, that any modelling tools could be chosen to be linked using the hybrid method. We chose here an example of the reflection of a shear wave from a planar crack. The shear wave was generated at a point in the Source domain and the crack was modelled in the Defect domain. By keeping a modest separation between the source and the crack, it was also possible, separately, to perform a single FE simulation of the whole process, thus enabling the numerical verification.

The procedure for the hybrid method is: 1) to simulate the generation of the wave field in the Source domain, 2) to estimate the resulting wave as it is incident on the Defect domain using the hybrid interface (the forward process), 3) to simulate reflection from the defect, 4) to estimate the reflected wave returning to the source location using the hybrid interface (the backward process). For the purpose of detailed verification, these forward and backward processes are demonstrated separately in the following subsections. The full process will later be validated as a whole against experiment.

For the forward process of the hybrid model, the incident wave field was taken from the boundary of the source box and then estimated on the exterior (excitation plane) of the defect box; similarly, for the backward process, the reflected wave field was estimated at the receiver based on the scattered signal on the boundary of the defect box. Here we use ”box” to refer to the cuboid at the exterior of the region of interest of each domain; the domains were larger than this because they contained absorbing material outside the region of interest.

The reference case to which the hybrid simulation was compared was a highly resolved large FE model including both the source and the defect. The incident and the reflected time signals were monitored at locations within this model that corresponded to the boxes of the hybrid model; we refer to these as the Source and Defect Monitoring Cuboids (SMC and DMC) respectively. We call this model, including both source and defect, the ‘Full FE’ model, and the monitored signal was the reference against which we tested the corresponding hybrid simulation.

This problem has been modelled at an arbitrary scale, but since the material is perfectly elastic the identical results can be obtained at any chosen consistent scale of distance and frequency. Therefore, the results here are scaled to dimensions and frequencies that are relevant for cases of interest to non destructive evaluation. According to this scale, a domain of dimension 60 by 48 by 48 mm is selected, and two models are considered, one without a crack and the other including a smooth flat square crack of dimension 3.2 by 3.2 mm. Fig. 2 shows the geometry of the domain and the location of the crack. The models were set up using the ABAQUS [20] CAE. The model without the crack was used for the forward simulation while the model with the crack was used for the backward simulation. The domain was regularly meshed with linear hexahedral elements (C4D8R in ABAQUS) of nominal size 0.2 mm ($\approx \lambda_S/16$ at the center frequency of the signal). The outside of the domain was filled with absorbing layers [14], and the thickness of the absorbing region was selected to be approximately 18 mm $\approx 3\lambda_L$, resulting in over 90 $\%$ of the calculation volume being occupied by the absorbing region. A point source of Hanning-windowed 5-cycle toneburst of 1 MHz centre frequency was used for the shear wave excitation. The rectangular crack was facing the excitation point which was 12 mm ($\approx 4\lambda_S$) from the crack, and was created by disconnecting elements so that it had no volume. Aluminium (Young’s modulus 71GPa, density 2700 kg/m^3 and Poisson ratio 0.33) was used for the material. The SMC surrounded the point source and each of its six surfaces was 6 mm $\times$ 6 mm in size, and the DMC was the same size, surrounding the centre of the rectangular crack as shown in Fig. 2.

The linking process was conducted at a set of frequency points, then Fast Fourier Transforms (FFT) and Inverse Fast Fourier Transforms (IFFT) were used to calculate the time-domain signals. Thus, a frequency region of interest had to be selected, for which the range 0.2 - 1.8 MHz was chosen for the following examples, covering the main lobe near 1 MHz and two side lobes on both sides of the main lobe.

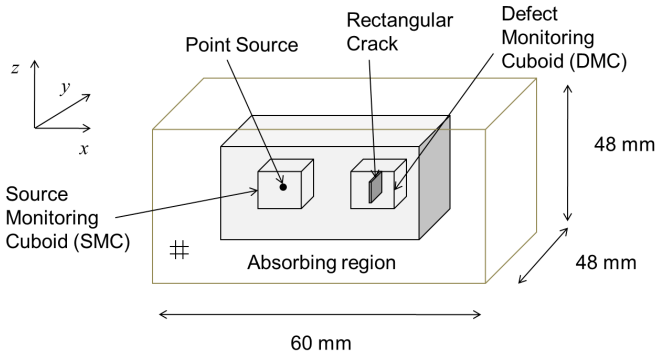

Fig. 2: Geometry for the numerical example of reflection of a shear wave from a planar crack

A. *Forward propagator*

In this first step, the hybrid method was used to estimate wave propagation from the point source in the forward process, for which incident wave propagation, in the defect domain, but without a crack, was simulated so that there was no reflection. Displacements and stresses were monitored at nodes on the SMC shown in Fig. 3(a), for input to the hybrid interface, and also at the DMC shown in Fig. 3(b), for comparison. Displacements u^{in} at nodes on the DMC were estimated separately via the hybrid interface, based on the SMC monitored signal. Fig. 4 shows the incident waves at a node on the DMC, predicted using the hybrid interface and the Full FE result and normalized by the incident amplitude at the source point. They agree well with each other in both the time and frequency domains, although for the first and the last lobe in Fig. 4(b) there is some small (note this is shown on a logarithmic scale) disagreement since they are out of the chosen frequency range for the FFT/IFFT.

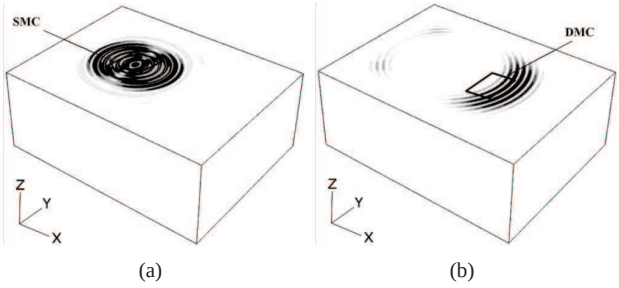

Fig. 3: Cross-sectional view of Full FE model for forward process, showing (a) wave shortly after being generated, just leaving the SMC, and (b) wave sometime later, passing over the DMC. This is the example without the defect present, so there is no scattering yet. The cross-section is a horizontal plane cut through the middle of the Full FE model. The polarisation of the shear wave is such that its motion is in the Y direction.

B. *Backward propagator*

For the backward process, the simulation was repeated but now with the crack in the Defect domain, and displacements and stresses were again monitored at nodes on the SMC and DMC in the Full FE model. The total displacement includes

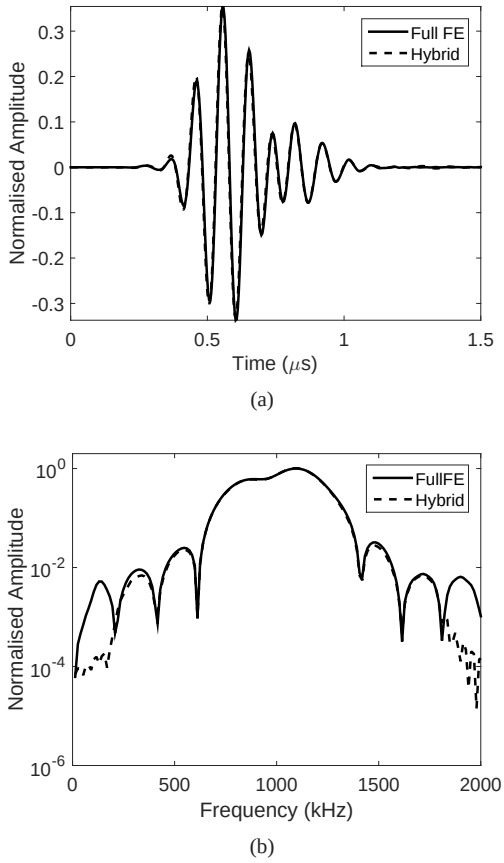

Fig. 4: Y direction displacement at an arbitrary point on DMC (a) in the time domain (b) in the frequency domain from Full FE (solid line) and Hybrid (dashed line) models. The time domain results are indistinguishable on this scale, while the frequency domain results show observable differences only outside the frequency range of the calculations.

the components of the incident and reflected wave fields, $u^{\text{tot}} = u^{\text{in}} + u^{\text{ref}}$, as is seen in illustration in Fig. 5(a). However, only the reflected wave is required to be fed into the hybrid interface and thus the reflected field was calculated as $u^{\text{ref}} = u^{\text{tot}} - u^{\text{in}}$ using the results from the model without a defect in the previous section.

The estimated reflection at an arbitrary point on the SMC is shown in Fig. 6. In both the time and frequency domains, only the reflected field is shown for the hybrid method, while the signal from the Full FE model also includes the incident wave component. Accordingly, the hybrid model correctly shows zero displacement in the first part of the time record, corresponding to the incident signal on its way towards the crack, while the Full FE model shows its highest amplitude here. At a later time, corresponding to the reflected signal, both models show good agreement. There is a small but observable difference between the full FE and the hybrid results in Fig. 6(a), which is due to spatial and time discretization and will be explained in Section. V-C.

V. Experimental validation

For an experimental validation we have chosen the reflection of a compression wave from a Side Drilled Hole (SDH).

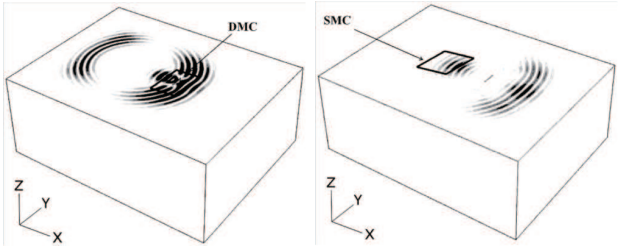

Fig. 5: Cross-sectional view of Full FE model for the backward propagation study, shown on same cross-section as in Fig. 3. Now, in (a), the wave reflected from the crack can be seen shortly after reflection, just as it crosses the DMC, and in (b) it can be seen sometime later passing into the SMC.

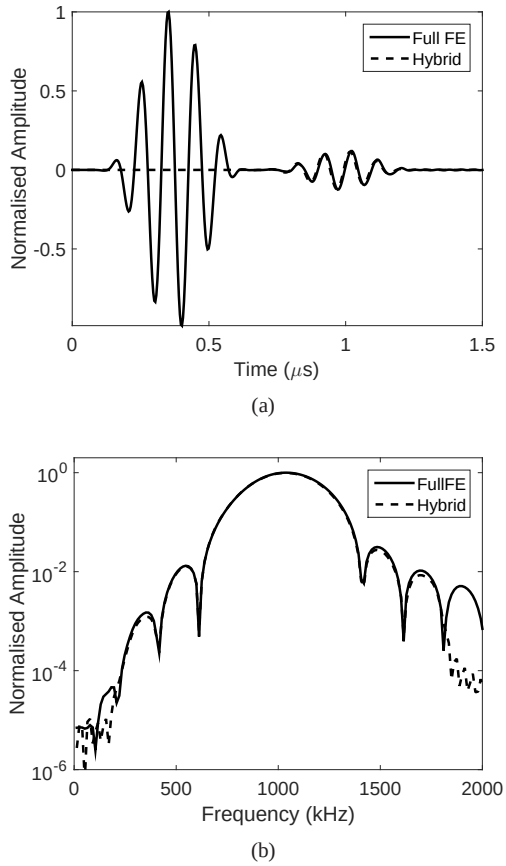

Fig. 6: Y direction displacement at an arbitrary point on SMC (a) in the time domain (b) in the frequency domain from Full FE (solid line) and Hybrid (dashed line) models. Only the reflected signal is shown for the Hybrid method, while the signal from the Full FE model also includes the incident wave component. This is why the Hybrid result shows zero displacement in the first part of the time record (a), corresponding to the incidence of the wave before reaching the defect, while both models agree well later in time when the reflected signal arrives.

Whereas this is a geometrically simple case compared to the complex defects that might be modelled using the hybrid method, it is an interesting and relevant one because the SDH is widely used to obtain quantifiable reference signals in ultrasonic NDE inspection. In this section, the three cases of

experiment, large FE model, and Hybrid method are described and the results are then compared.

A. *Experiment*

A 60 mm-thick stainless steel test block was selected for this experiment, having four 3-mm SDHs located at 5, 15, 25 and 45 mm from the transducer, as shown in Fig. 7. A 0.5-inch (12.5-mm) circular broadband transducer with a nominal centre frequency of 2.25MHz (GE MSWQC (SE0599)), was used to generate a compression wave, and it was excited by applying a short-time voltage pulse to the piezoelectric crystal. The pulse width of the DC voltage was equal to the duration (222ns) of half a cycle at the centre frequency. The data was acquired using a FMC Micropulse manufactured by PeakNDT, with the pulse-echo time history acquired through a single channel. The time history was recorded at lateral locations along the top of the block from 0mm to 66mm, at 1 mm increments, and each time record was digitised at a sampling frequency of 10MHz. This ensured thorough coverage of the test block, with data that was acquired in a practical time period.

Upon examining the response from the back wall, it was found that the centre frequency of the transducer was 2.6MHz, differing, as is common in practice, from the nominal specification of 2.25MHz; accordingly the simulations that follow were made using a centre frequency of 2.6MHz.

The setup for the ultrasonic test is shown in the schematic diagram in Fig. 7(a), and the reflections from the four SDHs and the backwall are seen from the "B-scan" in Fig. 7(b); in this plot the x axis shows the lateral position of the transducer on the top of the block, the y axis shows the distance of propagation calculated from the time record according to the known wave speed, and the grey scale shows the amplitude of the signal. The wave speed that was used for that calculation was based on the material properties of stainless steel: density 8000 Kg/m^3, Young's modulus 200 GPa, and Poisson ratio 0.3.

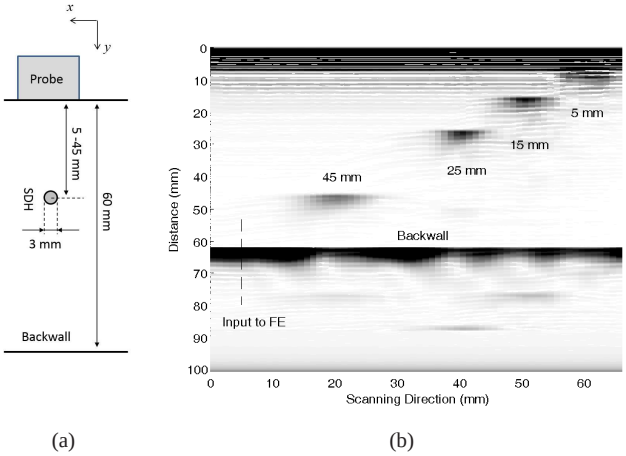

Fig. 7: Side Drilled Hole (SDH) Experiment, (a) schematic diagram of the experiment and (b) B-scan signal in the experiment showing reflections from SDHs at 5, 15, 25, and 45 mm. Dashed line shows where the input waveform is extracted for simulations

B. *Full FE model*

A domain including both the transducer and the SDH was modelled for comparison, in which all the wave propagation and reflections were simulated using only one FE model. This used a quarter-symmetric model as shown in Fig. 8 in order to reduce the size of the domain. The quarter symmetry is justified because the transducer, the SDH and the wave field possess this symmetry. In order to achieve this, the x and z direction displacements were set to be zero at the $x = 0$ and $z = 0$ plane, respectively. The term "Full FE" model will be used for this quarter model throughout this paper, to distinguish it from the hybrid model.

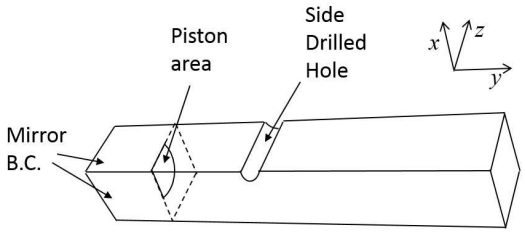

Fig. 8: Schematic of the "Full FE" model that was used to simulate the compression wave reflection from the SDH, including representation of both the transducer and the SDH. As can be seen by the region shown in the figure, it was possible to make use of an economy of quarter symmetry in order to reduce the spatial domain of the model.

The stainless steel test block was modelled using density 8000 Kg/m^3, Young's modulus 200 GPa, and Poisson ratio 0.3, and meshed by linear hexahedron elements (C4D8R in ABAQUS) of nominal length 0.1 mm ($\approx \lambda_L/22$). Three separate full FE models with the SDH at a distance of 15, 25, and 45 mm, respectively, were simulated with sections of up to 10.8 $\times$ 10.8 $\times$ 55.3 mm^3 domain size. The region near the SDH was meshed by sweeping free surface meshes along the axis of the hole, but the other regions were regularly meshed using ABAQUS CAE. For the exterior absorbing region, a recently-developed variant of the absorbing regions method, called Stiffness Reduction Method (SRM) [15], was implemented, which enabled the thickness of the absorbing material to be reduced to 1.5 λ_L. The circular transducer was simulated by a quarter-circular piston, and thus nodes within a 6.4 mm radius on a plane were selected, to all of which an identical excitation waveform was applied. The time signal at the receiver was obtained by averaging the y direction displacement at the nodes on the piston.

In general, it is difficult to obtain the actual waveform of the input signal used in an experiment for use as input to the simulation. For this simulation, the reflection from the backwall (see Fig. 7) of the test block was measured, corresponding to the location shown by the dashed line in part (b) of the figure. Its time trace was used for the input waveform of the simulation, after removing its DC offset, and this is shown in Fig. 9(a). An ideal toneburst should show approximate symmetry in the time domain, such as the incident signal in Fig. 6(a), but this signal shows a relatively steep rise at the start of the signal; this can be seen more clearly by looking at the signal envelope (Hilbert transform)

in Fig. 9(b). This sharp rise includes energy over a larger frequency range than would be expected from the ideal narrow band toneburst considered earlier, and this required a relatively wide range of frequency to be covered by the simulations, as will be shown shortly.

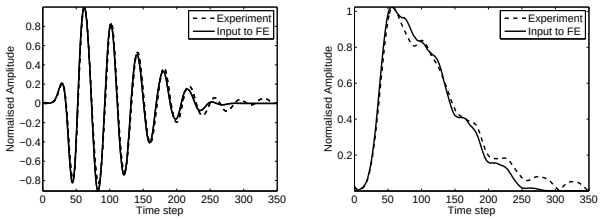

(a) (b)

Fig. 9: Waveforms (a) in the time domain and (b) their envelopes (Hilbert transform). The dashed line, taken from the measurements at the dashed line in Fig. 7(b) of the B-scan experiment, has been modified for input to the simulation by setting the DC offset to zero. The signal thus modified is shown by the solid line.

C. *Hybrid estimation*

For the Hybrid simulations, reflection from SDHs at 15 and 25 mm distance were simulated with two physically separated FE models, the Source and Defect domains, that were linked by the 3D Hybrid interface. Fig. 10 shows a schematic diagram of the two FE models. The Source domain of 21.6 $\times$ 8.8 $\times$ 21.6 mm^3 was regularly meshed for simulating the transducer excitation, and the absorbing regions were again deployed using the SRM method. Nodes within a 12.8 mm diameter in the middle of the plane perpendicular to the y direction were selected for the piston excitation. Inside the Source domain, an imaginary SMC surrounds the piston, 13.8 $\times$ 1 $\times$ 13.8 mm^3, and displacements at nodes on the SMC were monitored for use in the Hybrid link. In this model, for simplicity, only displacements on the SMC surface closest to the SDH were fed into the Hybrid interface, and thus the displacement on the other surfaces did not have an effect on the forward estimates. The frequency region of interest was selected to cover amplitudes larger than 5 % of the maximum amplitude in the frequency domain, and, as discussed ealier, this was necessary over a relatively wide frequency range to cover the bandwidth of the transducer. The frequency range that was covered was from about 0.5 to 4.5 MHz.

The Defect domain of 11.8 $\times$ 11.8 $\times$ 21.6 mm^3 was modelled for reflection from the SDH. Similar to the quarter FE model, sweep and regular meshes were used for this model. An imaginary DMC of 4 $\times$ 4 $\times$ 13.8 mm^3 was located in the center of the domain in order to monitor the time signal. Since the model has a hole through the surfaces normal to the *z* direction, the signal from these two surfaces was not considered in the backward Hybrid process. In order to simulate the incident wave from the Source domain, an excitation plane was located 0.3 mm behind the DMC in the *y* direction. By calculating only the longitudinal potential in the Hybrid method, only longitudinal waves were considered. One

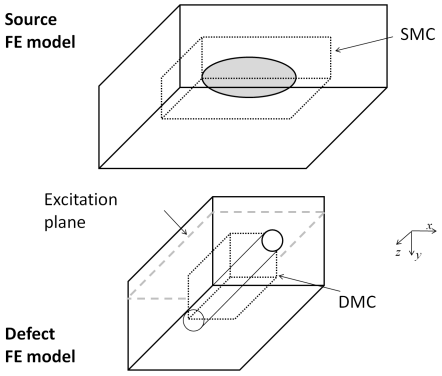

Fig. 10: Schematic diagram for Hybrid method, Source and Defect FE models.

of the main advantages of the Hybrid method is that different wave types can be separated in this way.

The hybrid and full FE results are compared in Fig. 11(a) for the case of the SDH at 15 mm depth, showing the time record of the amplitude of the signal at the transducer. The first part of the signal is the incident wave, which is represented completely by the full FE model, but is absent, as expected, from the hybrid model. The later part of the signal is the reflection from the SDH. The figure shows good agreement of the shape of the waveform, but the reflected signal in the hybrid model arrives slightly earlier than that in the full FE model. There is a good reason for this, which is the difference in wave speed in the open space between the transducer and the SDH. Whereas the hybrid model can assume the correct speed of bulk compression waves in the steel, the full FE model introduces an error because of its imprecise simulation of the speed of the wave over this distance. Explicit time domain simulation of waves incurs a speed error that is a function of the time step and element size [23], [24]. For this case the mesh density and timestep can be used to estimate the error [25], giving a value of about 0.5% delay at the centre frequency. Fig. 11(b) shows that compensation of the time by this percentage brings the signals into line. Thus the hybrid model has represented an improved solution in this respect in comparison to the full FE model.

Fig. 12 shows a comparison between the time records for the experimental, the full FE and the hybrid results with SDHs at 15 mm and 25 mm. The arrival time of the signal is expressed in distances based on the assumed wave speed. The amplitudes and the distances are normalized by the maximum amplitude and its location of backwall reflection, and the signals have been rectified, as is usual in industrial practice. The signal shapes are also well matched, now revealing additional content in the trailing part of the waveform that is characteristic of reflections from cylindrical holes and is quite different from the reflection from a flat face (compare with Fig. 9(b)). However there is a significant discrepancy in amplitude between simulations and experiment. There are several experimental uncertainties that could account for this but were not quantified, including the pressure profile across the face of the transducer, the quality of acoustic coupling between the transducer and the sample, and the registration of

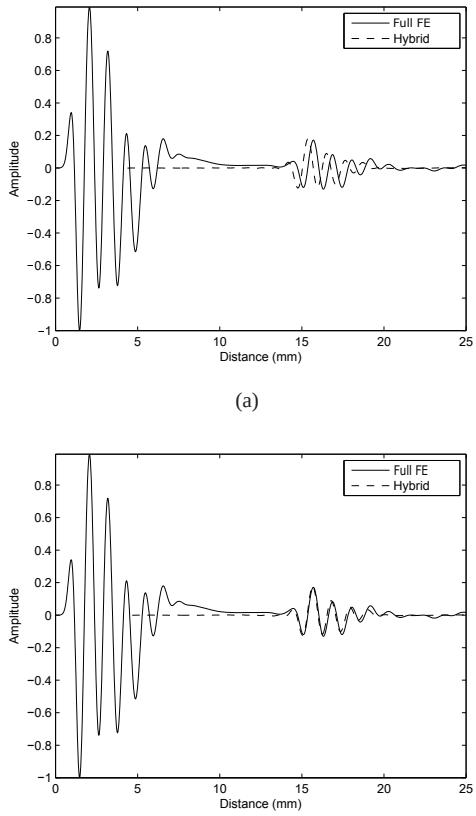

Fig. 11: Received signal at the transducer (a) before and (b) after the compensation

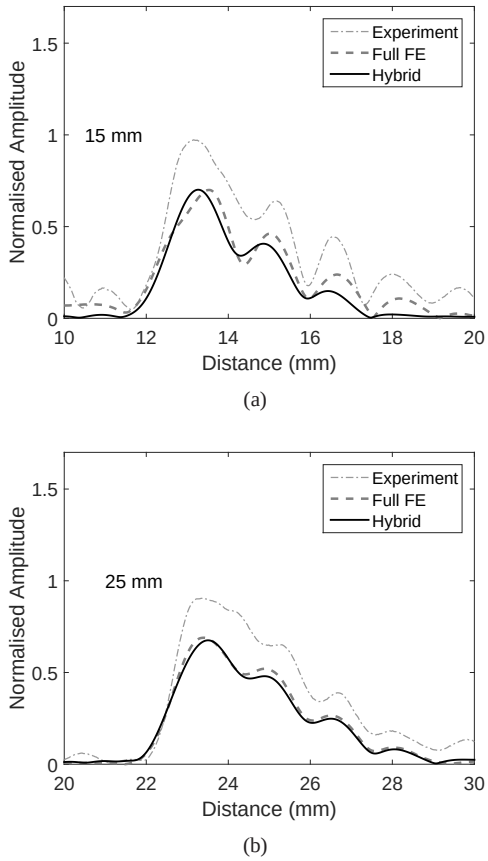

Fig. 12: Time records ("A-scans") from experimental measurement and the corresponding simulations using the Full FE and hybrid models for SDHs at distances of a) 15mm and b) 25mm. The *x* axis is mapped to equivalent distance from the transducer, using the assumed wave speed. Amplitudes and distances are normalized by the ones from the backwall at 60mm.

the lateral position of the transducer with respect to the SDHs.

Finally, the computation times are compared in Table I. Before discussing these it is important to understand that the purpose of the present paper is to enable a more efficient methodology, indeed a methodology that enables cases to be modelled that are simply not possible in full FE. Therefore the examples that we show here are primarily to illustrate the fact that the hybrid model costs the same computing resource for any chosen distance between transducer and defect, while the costs for a full FE model would increase sharply with increasing separation distance. Currently most of the examples here do not show reduced cost but we expect this to be achieved by future implementations, and we discuss the issues relating to this at the end of this section.

The times for the Full FE simulations are calculated by multiplying by 4 the time for the quarter simulation shown in Fig. 8 for comparison with the hybrid model shown in Fig.11, and the computation times in the hybrid model are shown for the two FE simulations for source and defect and the hybrid interface. The full FE and the hybrid simulation for 15 mm and 25 mm are executed on an identical machine and the time for 60 mm is estimated based on the 15 mm and 25 mm results. We also include an estimate for a case with a finer mesh. This is realistic for simulations of scattering from complex defects, such as rough cracks, for which we typically use a mesh refinement of 30 elements per wavelength [15]. We have estimated the costs based on that level of refinement. As can be seen in the table, whereas the computation times for Full FE at a given mesh refinement increase with the distances, those for the hybrid method do not increase since, in the hybrid method, the size of the FE domains and the calculation labour in the interface remain the same. Therefore, the hybrid model is more advantageous when the propagation distance is larger. In most of the hybrid results, calculation using the hybrid interface takes more time than Full FE does, but this is because the interface is coded using a high-level computer language, MATLAB, and is also not optimised for the hybrid calculation. However, when it is coded with a compiled language, for example C or Fortran, and optimised, then the total computation time will be significantly smaller. It was not the intention of this article to demonstrate such an optimised code, but rather to present the methodology for the approach; clearly there is much more that can be done subsequently by way of bespoke coding to speed up the calculation in an implementation developed for this specific real use in industry. These time comparisons do not yet fully show the advantages available using the hybrid model, and it is important to recognise the context. Firstly, in order to be

	Full FE	hybrid		
		FE	Interface	total
15 mm	640	60	2000	2060
25 mm	860	60	2000	2060
60 mm	1700	60	2000	2060
60 mm (fine mesh)	7080	250	2800	3050

TABLE I: Recorded and estimated computation times in minutes.

able to validate the hybrid model, the cases that have been simulated have deliberately used short propagation distances, so that it is possible to run the full model. However in real applications, such as the simulation of the NDE of small complex defects in thick-section components, it is often not possible to run the full model at all because of the limits of the computer memory. Therefore, in addition to the efficiency benefit for long distances that is shown in Table 1, there is also the consideration of what is actually possible to model and what is not. Secondly, there is much research interest in developing schemes to reduce the volume of the absorbing regions; when improvements are made to this they will make a substantial impact on reducing the calculation time of the hybrid solution.

VI. Conclusions

A 3D generic hybrid method has been developed for simulating 3D ultrasonic NDE inspection, which is a more realistic and practical modelling environment than 2D. The generality of our Hybrid method is that it can be applied to a wide range of NDE problems without modifying the simulation tools to be linked. The linking process has been described as well as the methodologies for its numerical implementation. Longitudinal scalar potential and shear vector potentials were defined, and the gauge condition, was used for deriving equations for the method. Examples of the hybrid link were presented assuming that displacements and stresses are typical outputs of candidate simulation schemes that might be used in the local domains that are to be linked. A verification of the 3D hybrid interface was executed by comparing with FE results, and the forward and backward estimates show good agreement with the FE results. The hybrid method was also compared with experiments with side drilled holes, demonstrating its practical use, and again showing good performance. It has been shown to be robust, including with respect to numerical errors such as the wave speed over long propagation distances which is adversely influenced in full FE modelling of large domains.

Appendix A
Equations of motion

For completeness, the equations of motion are presented. For clarity of exposition here, avoiding unnecessary constants in the analysis, dimensionless variables are used in which physical lengths are scaled relative to a chosen length h of the geometry, velocities are scaled relative to C_T, the shear wave speed, time is scaled relative to h/C_T, and stresses σ are scaled relative to a Lamé coefficient $\mu(=\rho C_T^2)$ of the material whose density is ρ. Hence, in dimensionless variables, with no external force, for time-harmonic elastic motion we can write the equations of motion in terms of displacements u and stresses $\tau(=\sigma/\mu)$,

$$-\omega^2 u_x = \frac{\partial \tau_{xx}}{\partial x} + \frac{\partial \tau_{xy}}{\partial y} + \frac{\partial \tau_{xz}}{\partial z}, \tag{20}$$

$$-\omega^2 u_y = \frac{\partial \tau_{xy}}{\partial x} + \frac{\partial \tau_{yy}}{\partial y} + \frac{\partial \tau_{yz}}{\partial z}, \tag{21}$$

$$-\omega^2 u_z = \frac{\partial \tau_{xz}}{\partial x} + \frac{\partial \tau_{yz}}{\partial y} + \frac{\partial \tau_{zz}}{\partial z}, \tag{22}$$

$$\tau_{xx} = \gamma^{-2}\frac{\partial u_x}{\partial x} + (\gamma^{-2}-2)\frac{\partial u_y}{\partial y} + (\gamma^{-2}-2)\frac{\partial u_z}{\partial z}, \tag{23}$$

$$\tau_{yy} = (\gamma^{-2}-2)\frac{\partial u_x}{\partial x} + \gamma^{-2}\frac{\partial u_y}{\partial y} + (\gamma^{-2}-2)\frac{\partial u_z}{\partial z}, \tag{24}$$

$$\tau_{zz} = (\gamma^{-2}-2)\frac{\partial u_x}{\partial x} + (\gamma^{-2}-2)\frac{\partial u_y}{\partial y} + \gamma^{-2}\frac{\partial u_z}{\partial z}, \tag{25}$$

$$\tau_{xy} = \frac{\partial u_y}{\partial x} + \frac{\partial u_x}{\partial y}, \tag{26}$$

$$\tau_{xz} = \frac{\partial u_x}{\partial z} + \frac{\partial u_z}{\partial x}, \tag{27}$$

$$\tau_{yz} = \frac{\partial u_y}{\partial z} + \frac{\partial u_z}{\partial y}. \tag{28}$$

Appendix B
Potentials on Region 1

Potentials on the boundary can be expressed as

$$\psi = \frac{1}{\omega^2}\left(\tau_{yz} - 2\frac{\partial u_y}{\partial z}\right),\ \chi = \frac{1}{\omega^2}\left(\frac{\partial u_x}{\partial z} - \frac{\partial u_z}{\partial x}\right),$$
$$\text{and } \eta = \frac{1}{\omega^2}\left(2\frac{\partial u_y}{\partial x} - \tau_{xy}\right) \quad \text{on } y = \text{constant} \tag{29}$$

$$\psi = \frac{1}{\omega^2}\left(2\frac{\partial u_z}{\partial y} - \tau_{yz}\right),\ \chi = \frac{1}{\omega^2}\left(\tau_{xz} - 2\frac{\partial u_z}{\partial x}\right),$$
$$\text{and } \eta = \frac{1}{\omega^2}\left(\frac{\partial u_y}{\partial x} - \frac{\partial u_x}{\partial y}\right) \quad \text{on } z = \text{constant}. \tag{30}$$

Normal derivatives of the potentials on the boundary can be expressed on constant y surfaces as

$$\frac{\partial \phi}{\partial y} = \frac{-1}{\omega^2}\left(\frac{\partial \tau_{xy}}{\partial x} + \frac{\partial \tau_{yz}}{\partial z} - 2\left(\frac{\partial^2 u_y}{\partial x^2} + \frac{\partial^2 u_y}{\partial z^2}\right) - \omega^2 u_y\right), \tag{31}$$

$$\frac{\partial \psi}{\partial y} = \frac{-1}{\omega^2}\left(\omega^2 u_z + \frac{\partial \tau_{xz}}{\partial x} + \frac{\partial \tau_{yy}}{\partial z} + 2\frac{\partial^2 u_z}{\partial z^2}\right), \tag{32}$$

$$\frac{\partial \chi}{\partial y} = \frac{1}{\omega^2}\left(\frac{\partial \tau_{xy}}{\partial z} - \frac{\partial \tau_{yz}}{\partial x}\right), \tag{33}$$

$$\frac{\partial \eta}{\partial y} = \frac{1}{\omega^2}\left(\omega^2 u_x + \frac{\partial \tau_{xz}}{\partial z} + \frac{\partial \tau_{yy}}{\partial x} + 2\frac{\partial^2 u_x}{\partial x^2}\right), \tag{34}$$

and on constant z surfaces as

$$\frac{\partial \phi}{\partial z} = \frac{-1}{\omega^2}\left(\frac{\partial \tau_{xz}}{\partial x} + \frac{\partial \tau_{yz}}{\partial y} - 2\left(\frac{\partial^2 u_z}{\partial x^2} + \frac{\partial^2 u_z}{\partial y^2}\right) - \omega^2 u_z\right), \tag{35}$$

$$\frac{\partial \psi}{\partial z} = \frac{1}{\omega^2}\left(\omega^2 u_y + \frac{\partial \tau_{xy}}{\partial x} + \frac{\partial \tau_{zz}}{\partial y} + 2\frac{\partial^2 u_y}{\partial y^2}\right), \tag{36}$$

$$\frac{\partial \chi}{\partial z} = \frac{-1}{\omega^2}\left(\omega^2 u_x + \frac{\partial \tau_{xy}}{\partial y} + \frac{\partial \tau_{zz}}{\partial x} + 2\frac{\partial^2 u_x}{\partial x^2}\right), \quad (37)$$

$$\frac{\partial \eta}{\partial z} = \frac{1}{\omega^2}\left(\frac{\partial \tau_{yz}}{\partial x} - \frac{\partial \tau_{xz}}{\partial y}\right). \quad (38)$$

APPENDIX C
STRESSES ON REGION 2

On constant *y* surfaces, using Eqs. (23) – (25) and (2),

$$\tau_{xx} = -\omega^2\gamma^2(\gamma^{-2} - 2)\phi + 2\frac{\partial u_x}{\partial x}, \quad (39)$$

$$\tau_{yy} = -\omega^2\phi - 2\left(\frac{\partial u_x}{\partial x} + \frac{\partial u_z}{\partial z}\right), \quad (40)$$

$$\tau_{zz} = -\omega^2\gamma^2(\gamma^{-2} - 2)\phi + 2\frac{\partial u_z}{\partial z}, \quad (41)$$

in which, for example,

$$\frac{\partial u_x}{\partial x} = \frac{\partial^2 \phi}{\partial x^2} + \frac{\partial^2 \eta}{\partial x \partial y} - \frac{\partial^2 \chi}{\partial x \partial z}, \quad (42)$$

and

$$\tau_{xy} = 2\frac{\partial^2 \phi}{\partial x \partial y} - \left(2\frac{\partial^2}{\partial x^2} + \frac{\partial^2}{\partial z^2} + \omega^2\right)\eta + \frac{\partial^2 \psi}{\partial x \partial z} - \frac{\partial^2 \chi}{\partial y \partial z}, \quad (43)$$

$$\tau_{xz} = 2\frac{\partial^2 \phi}{\partial x \partial z} + \frac{\partial^2 \eta}{\partial y \partial z} + \left(\frac{\partial^2}{\partial x^2} - \frac{\partial^2}{\partial z^2}\right)\chi - \frac{\partial^2 \psi}{\partial x \partial y}, \quad (44)$$

$$\tau_{yz} = 2\frac{\partial^2 \phi}{\partial y \partial z} - \frac{\partial^2 \eta}{\partial x \partial z} + \left(\frac{\partial^2}{\partial x^2} + 2\frac{\partial^2}{\partial z^2} + \omega^2\right)\psi + \frac{\partial^2 \chi}{\partial x \partial y}. \quad (45)$$

Similarly, on constant *z* surfaces,

$$\tau_{xx} = -\omega^2\gamma^2(\gamma^{-2} - 2)\phi + 2\frac{\partial u_x}{\partial x}, \quad (46)$$

$$\tau_{yy} = -\omega^2\gamma^2(\gamma^{-2} - 2)\phi + 2\frac{\partial u_y}{\partial y}, \quad (47)$$

$$\tau_{zz} = -\omega^2\phi - 2\left(\frac{\partial u_x}{\partial x} + \frac{\partial u_y}{\partial y}\right), \quad (48)$$

$$\tau_{xy} = 2\frac{\partial^2 \phi}{\partial x \partial y} + \left(\frac{\partial^2}{\partial y^2} - \frac{\partial^2}{\partial x^2}\right)\eta + \frac{\partial^2 \psi}{\partial x \partial z} - \frac{\partial^2 \chi}{\partial y \partial z}, \quad (49)$$

$$\tau_{xz} = 2\frac{\partial^2 \phi}{\partial x \partial z} + \frac{\partial^2 \eta}{\partial y \partial z} + \left(2\frac{\partial^2}{\partial x^2} + \frac{\partial^2}{\partial y^2} + \omega^2\right)\chi - \frac{\partial^2 \psi}{\partial x \partial y}, \quad (50)$$

$$\tau_{yz} = 2\frac{\partial^2 \phi}{\partial y \partial z} - \frac{\partial^2 \eta}{\partial x \partial z} - \left(\frac{\partial^2}{\partial x^2} + 2\frac{\partial^2}{\partial y^2} + \omega^2\right)\psi + \frac{\partial^2 \chi}{\partial x \partial y}. \quad (51)$$

REFERENCES

[1] E. I. Thorsos, "Validity of Kirchhoff approximation for rough surface," *Journal of the Acoustic Society of America*, vol. 83, no. 1, pp. 78 – 92, 1988.

[2] J. B. Keller, "Geometrical theory of diffraction," *Journal of the Optical Society of America*, vol. 52, no. 2, pp. 116 – 130, 1962.

[3] Y. P. Ufimstev, *Fundamentals of the physical theory of diffraction*. John Wiley & Sons, Inc., 2007.

[4] P. Calmon, S. Mahaut, S. Chatillon, and R. Raillon, "CIVA: An expertise platform for simulation and processing NDT data," *Ultrasonics*, vol. 44, pp. 975 – 979, 2006.

[5] J. M. Coffey and R. K. Chapman, "Application of elastic scattering theory for smooth flat cracks to the quantitative prediction of ultrasonic defect detection and sizing," *Nucl. Energy*, vol. 22, no. 5, pp. 319 – 333, 1983.

[6] P. Rajagopal and M. J. S. Lowe, "Scattering of the fundamental shear horizontal guided wave by a part-thickness crack in an isotropic plate," *The Journal of the Acoustical Society of America*, vol. 124, no. 5, pp. 2895–2904, 2008. [Online]. Available: http://scitation.aip.org/content/asa/journal/jasa/124/5/10.1121/1.2982410

[7] B. Chassignole, V. Duwig, M.-A. Ploix, P. Guy, and R. E. Guerjouma, "Modelling the attenuation in the ATHENA finite elements code for the ultrasonic testing of austenitic stainless steel welds," *Ultrasonics*, vol. 49, pp. 653–658, 2009.

[8] A. Velichko and P. D. Wilcox, "A generalized approach for efficient finite element modeling of elastodynamic scattering in two and three dimensions," *J. Acoust. Soc. Am.*, vol. 128, pp. 1004–1014, 2010.

[9] L. Moreau, A. Velichko, and P. D. Wilcox, "Accurate finite element modelling of guided wave scattering from irregular defects," *NDT & E International*, vol. 45, pp. 46–54, 2012.

[10] D. Givoli, "High-order local non-reflecting boundary conditions: a review," *Wave Motion*, vol. 39, pp. 319 – 326, 2004.

[11] M. Israeli and S. Orszag, "Approximation of radiation boundary conditions," *Journal of Computational Physics*, vol. 41, pp. 115–135, 1981.

[12] J.-P. Berenger, "A perfectly matched layer for the absorption of electromagnetic waves," *Journal of Computational Physics*, vol. 114, no. 2, pp. 185 – 200, 1994.

[13] W. Ke, M. Castaings, and C. Bacon, "3d finite element simulations of an air-coupled ultrasonic NDT system," *NDT & E International*, vol. 42, pp. 524–533, 2009.

[14] P. Rajagopal, M. Drozdz, E. A. Skelton, M. J. Lowe, and R. V. Craster, "On the use of absorbing layers to simulate the propagation of elastic waves in unbounded isotropic media using commercially available finite element packages," *NDT & E International*, vol. 51, pp. 30 – 40, 2012.

[15] J. Pettit, A. Walker, P. Cawley, and M. Lowe, "A stiffness reduction method for efficient absorption of waves at boundaries for use in commercial finite element codes," *Ultrasonics*, vol. 54, pp. 1868–1879, 2014.

[16] S. K. Datta, "Diffraction of plane elastic waves by ellipsoidal inclusions," *J. Acoust. Soc. Am.*, vol. 61, pp. 1432–1437, 1977.

[17] R. Paskaramoorthy, A. H. Shah, and S. K. Datta, "Scattering of flexural waves by a crack in a plate," *Engng. Frac. Mech.*, vol. 33, pp. 589–598, 1989.

[18] J. Zhu and A. H. Shah, "A hybrid method for transient wave scattering by flaws in composite plates," *Intl. J. Solids Struc.*, vol. 34, pp. 1719–1734, 1997.

[19] P. Rajagopal, E. Skelton, W. Choi, M. Lowe, and R. Craster, "A generic hybrid model for bulk elastodynamics, with application to ultrasonic non-destructive evaluation," *IEEE Transactions on Ultrasonics, Ferroelectrics and Frequency control*, vol. 59, pp. 1239–1252, 2012.

[20] *ABAQUS v6.12 Analysis User's Manual*, 2012, http://www.simulia.com.

[21] W. Lester and J. Schmerr, *Fundamentals of Ultrasonic Nondestructive Evaluation*. Plenum Press, 1998.

[22] E. Sternberg, "On the integration of the equations of motion in the classical theory of elasticity," *Archive for Rational Mechanics and Analysis*, vol. 6, no. 1, pp. 34–50, 1960.

[23] R. Courant, K. Friedrichs, and H. Lewy, "Über die partiellen differenzengleichungen der mathematischen physik," *Mathematische Annalen*, vol. 100, no. 1, pp. 32–74, 1928.

[24] K.-J. Bathe, *Finite Element Procedures*. Prentice Hall, 2006.

[25] M. Drozdz, "Efficient finite element modelling of ultrasound waves in elastic media," Ph.D. dissertation, Imperial College London, 2008.